Synthesis of Silica/Hydroxyapatite Nanocomposite by Mechanochemical Method

Ahmed Hannora (ahmed.hannora@suezuniv.edu.eg)
Suez University
M. M. Mostafa
Suez University

Research Article

Keywords: Silica/Hydroxyapatite, nanocomposites, mechanochemical process, corrosion resistance

Posted Date: May 28th, 2021

DOI: https://doi.org/10.21203/rs.3.rs-566561/v1

Abstract

Biocompatibility of Silica makes it a suitable material for biomedical applications. The main components of teeth and bones are calcium phosphate (CP). Hydroxyapatite (HA) is expected to be used in different fields not only in biomedical applications but also in agriculture as a fertilizer and pollution treatment. Various substitutions in the apatite lattice play a significant role in its properties. In the present work, Silica-50, 40, 30 and 25 mol.% Hydroxyapatite nanocomposites were prepared successfully by mechanochemical processing method. X-ray diffraction (XRD) and Fourier Transform Infrared (FT-IR) indicated that silica stimulates the HA decomposition to β-tricalcium phosphate (β-TCP). XRD of heat-treated compacted sample at 1200^{o}C confirmed β-TCP and calcium phosphate silicate phases formation. Mechanical properties decreased with decreasing HA content. Electrochemical impedance spectroscopy (EIS) results revealed that pure HA possess the highest resistivity to corrosion, while the silica/HA samples showed lower corrosion resistance. The polarization resistance increases with HA content.

Introduction

Biocompatible silica nanoparticles recently have intrinsic biologic activity to the skeleton and to improve bone forming makes it a suitable material for biomedical applications [1-4]. Inorganic calcium phosphate based bio-ceramics materials such as hydroxyapatite $Ca_{10}(PO_4)_6(OH)_2$ has received considerable attention for bone repair applications and dental implants [5]. Also, hydroxyapatite is a promising candidate of air, water and soil pollution treatment due to its great adsorption capacities and ion-exchange capability [6-8]. Hydroxyapatite nanowires composite effectively improve the electrochemical performance of the lithium-sulfur batteries [9]. Several methods have been investigated to prepare CP nanostructures [10-12]. Regardless of the researches, creative designed CP nanostructures have not been supplemented for the substantial applications [13,14]. The low dissolution of HA in the human body after implantation and fast release of calcium and phosphate ions from β-tricalcium phosphate when exposed to physiological fluids limit its use in clinical applications [15]. Significant research has been carried out for both cationic and anionic hydroxyapatite substitutions [16-19].

Hydroxyapatite and silica have been used as fillers for dental applications [20-22,12,17,23]. Even hydroxyapatite based composite resins are bioinert with hardness like natural teeth, its exhibit lower strength and higher failure rates. Silica is used as a reinforcing filler for dental applications. It improves the shrinkage of restorative composite resins [21]. Lower wear resistance and biocompatibility are the major shortcomings of composite resin. Hydroxyapatite whiskers and silica nanoparticles were bioactive [12,21]. Moreover, the silica addition as a silicon source to HA bio-ceramic materials is found to be essential for normal bone and connective tissue development. Addition of silica could reduce the HA grain size and stimulate the decomposition of HA to tricalcium phosphate (TCP) α- and β-TCP phases. [24,25]. HA-SiO_2 composites directly prepared by sintering the powders of HA mixed with silica [26]. Addition of silica to Polyvinyl alcohol/HA matrix presented an improved capacity for both loading and sustained release of vancomycin hydrochloride [27].

Nano-fillers have superior mechanical properties and enhanced bioactivity in comparison to conventional cement [11,10,12]. The two approaches of manufacturing nano-size particles are top-down and bottom-up. The top-down involves the production of nano materials from bulk material while bottom-up involves production of nano materials atom by atom [28]. Mechanochemical synthesis as a top-down method is a solid-state reaction process. The main advantages of mechanochemical synthesis method of ceramic powders are low cost, simplicity, lower temperature and produce large amounts of powder [29]. Silica-hydroxyapatite nanocomposite was synthesized with different methods; sol–gel technique [30,12], plasma sprayed [31], coprecipitation method [32].

Depending on the above considerations, the purpose of this study was to investigate the effect of mechanochemical method for incorporation of bioactive hydroxyapatite with high content silica. Also, to study the mechanical and electrochemical properties of the formed composite materials.

Materials And Samples

Silica powders and 50, 40, 30 and 25 mol.% commercial hydroxyapatite (purchased from Sigma-Aldrich -21223) were placed into high energy vibratory ball milling. The powder treated with hard steel balls for one hour, with the optimum balls to powder ratio equals to 20:1. As-prepared samples were uniaxial compacted at 5 ton/square inch into circular discs samples with. Compacted samples, 13 mm diameter and 3 mm height, were heat treated at different temperatures between 500 and 1200°C for one hour holding time.

The compositions and formed phases of the prepared and heat-treated samples were analyzed by X-Ray powder diffractometer, D5000 using Cu K_{α} radiation (wavelength l = 0.15406 nm) using with a nickel filter. The diffractometer was operated at 40 kV and 30 mA within range of 20° < 2q < 60° with 0.05 degree/sec. The obtained phases were determined by the comparison with the standard ICDD (JCPDS). Fourier Transform Infrared Spectrometer (FT-IR) was performed using (MAC, FT/IR-4100 type A). The measurements were carried out in transmission mode in the range (450–4000 cm^{-1}) at the resolution of 4 cm cm^{-1}.

The bulk density of the sintered samples was measured by Archimedes' method, with Toluene as the immersion media. The contact angles of the deionized water on dried samples were determined in atmospheric condition at 25^{o}C using a sessile drop measurement. HWDV-7S Vickers microhardness tester was used for experimental indentation tests, under applied load 4.9N with dwelling time from 10 s to 15 s.

SP-300 Biologic workstation (France) was used for the electrochemical measurements using standard three-electrode cell. The electrochemical properties of the samples were examined in Ringer's solution with composition: 8.69 g/L NaCl (Na^{+} ~147.5 mEq/L), 0.3 g/L KCl (K^{+} ~4.0 mEq/L) and 0.48 g/L $CaCl_2$ (Ca^{++} 4mEq/L) at 35 ± 1 °C. PEIS test was performed from 10 mHz to 100 kHz . The parameters of

corrosion were calculated by using EC-Lab software V11.12 directly by curve fitting of the Tafel curve method. The specimen area exposed to the Ringer's solution was 0.785 cm^2.

Results And Discussion

Figure 1 shows XRD patterns of silica and HA without additives and that obtained after one-hour mechanical treatment by high energy ball. The intensity of the HA peaks decreases sharply after mechanical treatment while silica peaks slightly affected. With increasing silica content, the HA degree of crystallinity decreases. Same peaks related to rhombohedral beta tricalcium phosphate β-$Ca_3(PO_4)_2$ (JCPDS # 00-009-0169) phase appeared at 2θ equal 25.80, 27.77, 31.03 and 34.37°. The contribution of beta tricalcium phosphate (β-TCP) phase nearly the same with different HA content. The broadening of silica peaks increases as a result of induced severe plastic deformation and the particle size accordingly decreases. Through the milling process of this brittle–ductile system, fine hard silica powder dispersed in a ductile HA and the whole system particles becomes work hardened after mechanical treatment forming ultrafine powder. During the mechanical treatment intense impulsive forces induce severe plastic deformation energy transferred to HA which then transformed into β-TCP phase.

According to Roh et al., [33] tricalcium phosphate, have become preferred bone graft materials of choice.

Fig. 2 shows the FT-IR spectrum of silica with different HA content after mechanical treatment. The broad band detected at 3452 cm^{-1} corresponding to stretching vibration band of H_2O molecules (OH^- group) while band at 1636 cm^{-1} due to its bending vibration. The strong bands at 896 cm^{-1} (υ_1), 1098 cm^{-1} (υ_2), 1039 cm^{-1} (υ_3) and 566 cm^{-1} (υ_4) are due to vibrational mode present for phosphate groups of HA (PO_4^{3-} group). With increasing silica content, the 1098 cm^{-1} band intensity increases due to silica incorporation in hydroxyapatite matrix. The strong band at 1099 cm^{-1} with a shoulder at 1183 cm^{-1} is assigned to asymmetric stretching vibrations modes of the Si-O-Si, while the band at 469 cm^{-1} is due to O-Si-O bending vibrations. The symmetric stretching vibrations band of Si-O-Si was detected at 791 cm^{-1}. The intensity of these band gradually increases with increasing silica content. Compared with, [34,31,24,12], these values are very close to the recorded.

After heat treatment of the as-milled sample, the intensity of HA diffraction peak gradually decreased until it disappeared, and the β-TCP intensity increased. With increasing HA content, β-TCP phase gradually increases. The accumulation of defects into the crystalline lattice of silica/HA system give rise to locally distorted structures which enhance the chemical reactivity of the system. Beside the silica and β-TCP phase (decomposition product of HA with mechanical and heat treatment), silica could continue to react with HA forming monoclinic calcium silicate $CaSiO_3$ (JCPDS # 01-075-1396) and orthorhombic calcium phosphate silicate $Ca_5(PO_4)_2SiO_4$ (JCPDS # 00-040-0393). With increasing sintering temperature from 900°C to 1200°C, all the formed phases still found with higher quality.

In ionic materials solid-state reactions take place by the diffusion of ions across the interface. Pure HA partially transformed to β-TCP when sintered at 1100°C according to the following reaction, equation (1) [35];

$$Ca_{10}(PO_4)_6(OH)_2 \rightarrow 3Ca_3(PO_4)_2 + CaO + H_2O \quad (1)$$

Calcium silicate (*β*-wollastonite) is formed from CaO and SiO_2 at 900°C. The following reaction explain the calcium silicate phase formation, equation (2) [36];

$$CaO + SiO_2 \rightarrow CaSiO_3 \quad (2)$$

From the XRD patterns, Fig. 3 CaO phase was not detected sample with HA additives which means that all the CaO formed reacted with SiO_2 to form calcium silicate.

Crystallite size is a critical feature of nanomaterials that have a highly crystalline structure. Mechanical milling/alloying and mechanochemical treatment involves repeated fracturing and cold welding of the treated powder particle. Through the process crystallite size of the deformed powder decrease while accumulated strain, and dislocations increases. From the XRD analysis of line broadening, the estimated average crystallite size (D) of heat-treated samples can be calculated from the Scherrer's equation [37]:

$$D = \frac{k\lambda}{\beta \cos\theta} \quad (3)$$

where, β is the X-ray diffraction line broadening, θ is the Bragg's diffraction angle, k is the shape factor (0.9), and λ is the wavelength of Cu-k_α radiation (0.154 nm). Table 1 shows average crystallite size determined from Scherrer's equation of heat-treated Silica/HA samples at different temperatures.

Table 1 Crystallite size variation with different HA content and temperatures

HA content mol.%	Crystallite Size (nm)			
	800°C	900°C	1000°C	1200°C
50	71.6	94.1	171.7	174.5
40	66.9	121.5	196.3	203.1
30	69.6	130.3	206.6	215.8
25	82.7	138.6	211.3	221.3

Table 2 shows the mechanical properties of silica/HA system after heat treatment at 1200°C by using Vickers hardness number which calculated from equation (4) and (5) [38,39];

$$H_V = 0.1891 \frac{P}{d^2} \quad (4)$$

where P is the applied force (in N) and d the diagonal length (in mm) of the indentation. Yield stress (σ) can be approximated from the Hv values by [40];

$$\sigma = Hv/0.3 \quad (5)$$

Table 2 Mechanical properties of silica/HA system after heat treatment at 1200°C

HA content mol.%	Density gm/cm^3	Hardness, [Hv]	Hardness, [GPa]	Yield stress [MPa]
100	3.09	457.6	4.489	1525.3
50	2.998	342.7	3.362	1142.2
40	2.971	275.4	2.702	918.1
30	2.949	233.5	2.290	778.2
25	2.939	206.4	2.025	688.0

Density and micro hardness increased with higher content of HA. According to [41], the maximum hardness of sintered β-TCP obtained at 1100 °C was 240 HV for green pressed sample at 3 ton /square inch while [42] the maximum hardness of 407 HV appeared at 900 °C, then decreased with increasing sintering temperatures for green pressed sample at 1.5 ton /square inch. According to [43], hardness of 860 HV appeared at 1150 °C of green pressed sample at ~ 4 ton/square inch. Hardness of pure silica is 8 GPa [44].

Polarization curves and electrochemical impedance spectra (EIS) measurements were verified in Ringer's simulated physiological solution. According to Tafel's law, in an electrochemical reaction, the logarithm of the current density varies linearly with the electrode potential. Fig. 4 reveals anodic and cathodic Tafel polarization curves of HA and Silica/HA samples. As shown large anodic passive regions can be observed on the anodic branches of potentiodynamic curves of lower HA content samples. The cathodic processes with small slopes of the cathodic branches were under kinetic control while anodic processes can be considered mixed kinetic and diffusion controlled due to their large slope. Similar results have been reported in [45]. From the intersection of the anodic and cathodic lines extrapolation, the corrosion potential (E_{corr}) and corrosion current (i_{corr}) were calculated. The values of corrosion potential, corrosion current and corrosion rate are listed in Table 3.

Fig. 5 shows the Bode and Bode-phase plot of heat-treated HA and Silica/HA samples at 1200°C. The impedance modulus |Z| of Silica/HA samples decreases with frequency and increases with HA content, Fig. 5a. The Bode phase angle peak decreases with HA addition and shifted to the lower frequency values, Fig. 5b. Fig. 5c shows Nyquist graph where the real and the imaginary parts of complex impedance are plotted. Nyquist plots shows a semicircle with high frequency range for HA and Silica/HA samples. the largest semicircle verifies low ion release rate. Higher HA content samples have a lower degradation rate in Ringer's solution. The polarization resistance ($\mathbf{R_p}$) increases with HA content.

Table 3 Corrosion parameters of of heat-treated HA and Silica/HA samples at 1200°C

HA content mol.%	$E_{corr.}$ (mV)	$I_{corr.}$ (µA)	B_a (mV)	B_c (mV)	C_r (mmpy)	R_p (ohm)
100	-176.1	0.176	179.2	291.4	0.0451	29773
50	-148.3	0.764	180.4	189.2	0.1444	15358
40	-163.3	1.172	313.4	322.3	0.4068	8366
30	-202.4	1.831	321.5	331.3	0.4826	3889
25	-160.9	4.478	221.7	334.9	0.7739	1308

Conclusion

Nano crystalline Silica/HA composite successfully prepared by mechanochemical process. After heat treatment of Silica/HA samples, XRD results confirmed that the Silica/HA structure consisted of beta tricalcium phosphate, calcium phosphate silicate. Dense ceramics were obtained for Silica/HA after sintering at 1200°C. Pure HA showed a good corrosion resistance more than Silica/HA samples. Higher HA content samples have a lower degradation rate in Ringer's solution. The polarization resistance (R_p) increases with HA content. The mechanical properties decreased with increasing silica content.

Declarations

All authors declare that they have no known competing financial interests or personal relationships that could have appeared to influence the work reported in this paper.

This study was not funded.

References

1. Ha, S.-W., Viggeswarapu, M., Habib, M.M., Beck, G.R.: Bioactive effects of silica nanoparticles on bone cells are size, surface, and composition dependent. Acta Biomaterialia **82**, 184-196 (2018). doi:https://doi.org/10.1016/j.actbio.2018.10.018
2. Ha, S.-W., Weitzmann, M.N., Beck, G.R.: Chapter 4 - Dental and Skeletal Applications of Silica-Based Nanomaterials. In: Subramani, K., Ahmed, W., Hartsfield, J.K. (eds.) Nanobiomaterials in Clinical Dentistry. pp. 69-91. William Andrew Publishing, (2013)
3. Eivazzadeh-Keihan, R., Chenab, K.K., Taheri-Ledari, R., Mosafer, J., Hashemi, S.M., Mokhtarzadeh, A., Maleki, A., Hamblin, M.R.: Recent advances in the application of mesoporous silica-based nanomaterials for bone tissue engineering. Materials Science and Engineering: C **107**, 110267 (2020). doi:https://doi.org/10.1016/j.msec.2019.110267
4. Mondal, S., Hoang, G., Manivasagan, P., Moorthy, M.S., Kim, H.H., Vy Phan, T.T., Oh, J.: Comparative characterization of biogenic and chemical synthesized hydroxyapatite biomaterials for potential

biomedical application. Materials Chemistry and Physics **228**, 344-356 (2019). doi:https://doi.org/10.1016/j.matchemphys.2019.02.021

5. Sopcak, T., Medvecky, L., Girman, V., Durisin, J.: Mechanism of precipitation and phase composition of CaO–SiO2–P2O5 systems synthesized by sol–gel method. Journal of Non-Crystalline Solids **415**, 16-23 (2015). doi:https://doi.org/10.1016/j.jnoncrysol.2015.02.014
6. Ibrahim, M., Labaki, M., Giraudon, J.-M., Lamonier, J.-F.: Hydroxyapatite, a multifunctional material for air, water and soil pollution control: A review. Journal of Hazardous Materials **383**, 121139 (2020). doi:https://doi.org/10.1016/j.jhazmat.2019.121139
7. Márquez Brazón, E., Piccirillo, C., Moreira, I.S., Castro, P.M.L.: Photodegradation of pharmaceutical persistent pollutants using hydroxyapatite-based materials. Journal of Environmental Management **182**, 486-495 (2016). doi:https://doi.org/10.1016/j.jenvman.2016.08.005
8. Ferri, M., Campisi, S., Scavini, M., Evangelisti, C., Carniti, P., Gervasini, A.: In-depth study of the mechanism of heavy metal trapping on the surface of hydroxyapatite. Applied Surface Science **475**, 397-409 (2019). doi:https://doi.org/10.1016/j.apsusc.2018.12.264
9. Li, R., Sun, X., Zou, J., He, Q.: Hydroxyapatite nanowires composite interlayer based on aramid fiber paper for Li-S batteries. Journal of Electroanalytical Chemistry **856**, 113662 (2020). doi:https://doi.org/10.1016/j.jelechem.2019.113662
10. Huang, S.B., Gao, S.S., Yu, H.Y.: Effect of nano-hydroxyapatite concentration on remineralization of initial enamel lesionin vitro. Biomedical Materials **4**(3), 034104 (2009). doi:10.1088/1748-6041/4/3/034104
11. Najeeb, S.K., Z.; Zafar, M.S.; Khan, A.S.; Zohaib, S.; Martí, J.M.N.; Sauro, S.; Matinlinna, J.P.; Rehman, I.U. : Modifications in Glass Ionomer Cements: Nano-Sized Fillers and Bioactive Nanoceramics. International Journal of Molecular Sciences **17**(7), 1134 (2016). doi:10.3390/ijms17071134
12. Moheet, I.A., Luddin, N., Ab Rahman, I., Masudi, S.a.M., Kannan, T.P., Abd Ghani, N.R.N.: Evaluation of mechanical properties and bond strength of nano-hydroxyapatite-silica added glass ionomer cement. Ceramics International **44**(8), 9899-9906 (2018). doi:https://doi.org/10.1016/j.ceramint.2018.03.010
13. Yamada, S., Nishikawa, M., Tagaya, M.: Mesoporous silica formation on hydroxyapatite nanoparticles. Materials Letters **211**, 220-224 (2018). doi:https://doi.org/10.1016/j.matlet.2017.10.009
14. Martins, M.L., Iessi, I.L., Quintino, M.P., Damasceno, D.C., Rodrigues, C.G.: Glucose is an active chemical agent on degradation of hydroxyapatite nanostructure. Materials Chemistry and Physics **240**, 122166 (2020). doi:https://doi.org/10.1016/j.matchemphys.2019.122166
15. Song, C.-W., Kim, T.-W., Kim, D.-H., Jin, H.-H., Hwang, K.-H., Lee, J.K., Park, H.-C., Yoon, S.-Y.: In situ synthesis of silicon-substituted biphasic calcium phosphate and their performance in vitro. Journal of Physics and Chemistry of Solids **73**(1), 39-45 (2012). doi:https://doi.org/10.1016/j.jpcs.2011.09.021
16. Shepherd, J.H., Shepherd, D.V., Best, S.M.: Substituted hydroxyapatites for bone repair. Journal of Materials Science: Materials in Medicine **23**(10), 2335-2347 (2012). doi:10.1007/s10856-012-4598-2

17. Carvalho, E.V., de Paula, D.M., Andrade Neto, D.M., Costa, L.S., Dias, D.F., Feitosa, V.P., Fechine, P.B.A.: Radiopacity and mechanical properties of dental adhesives with strontium hydroxyapatite nanofillers. Journal of the Mechanical Behavior of Biomedical Materials **101**, 103447 (2020). doi:https://doi.org/10.1016/j.jmbbm.2019.103447
18. Duraia, E.-S.M., Hannora, A., Mansurov, Z., Beall, G.W.: Direct growth of carbon nanotubes on hydroxyapatite using MPECVD. Materials Chemistry and Physics **132**(1), 119-124 (2012). doi:https://doi.org/10.1016/j.matchemphys.2011.11.006
19. Hannora, A.E.: Preparation of calcium manganese phosphate by mechanochemical synthesis of manganese and hydroxyapatite. Journal of the Australian Ceramic Society **55**(3), 807-815 (2019). doi:10.1007/s41779-018-00293-4
20. Gu, Y.W., Yap, A.U., Cheang, P., Khor, K.A.: Effects of incorporation of HA/ZrO(2) into glass ionomer cement (GIC). Biomaterials **26**(7), 713-720 (2005). doi:10.1016/j.biomaterials.2004.03.019
21. Chadda, H., Naveen, S.V., Mohan, S., Satapathy, B.K., Ray, A.R., Kamarul, T.: Cytotoxic evaluation of hydroxyapatite-filled and silica/hydroxyapatite-filled acrylate-based restorative composite resins: An in vitro study. Journal of Prosthetic Dentistry **116**(1), 129-135 (2016). doi:10.1016/j.prosdent.2015.12.013
22. Felemban, N., Ebrahim, M.: Effects of adding silica particles on certain properties of resin-modified glass-ionomer cement. European Journal of Dentistry **10**, 225 (2016).
23. Hannora, A.E., Mukasyan, A.S., A., M.Z.: Nanocrystalline hydroxyapatite/Si coating by mechanical alloying technique. Bioinorganic Chemistry and Applications **2012**(2012), 1-14 (2012). doi:10.1155/2012/390104
24. Jia, Z.-Q., Guo, Z.-X., Chen, F., Li, J.-J., Zhao, L., Zhang, L.: Microstructure, phase compositions and in vitro evaluation of freeze casting hydroxyapatite-silica scaffolds. Ceramics International **44**(4), 3636-3643 (2018). doi:https://doi.org/10.1016/j.ceramint.2017.11.114
25. Moldovan, M., Prodan, D., Sarosi, C., Carpa, R., Socaci, C., Rosu, M.-C., Pruneanu, S.: Synthesis, morpho-structural properties and antibacterial effect of silicate-based composites containing graphene oxide/hydroxyapatite. Materials Chemistry and Physics **217**, 48-53 (2018). doi:https://doi.org/10.1016/j.matchemphys.2018.06.055
26. Li, X.W., Yasuda, H.Y., Umakoshi, Y.: Bioactive ceramic composites sintered from hydroxyapatite and silica at 1200∘C: preparation, microstructures and in vitro bone-like layer growth. Journal of Materials Science: Materials in Medicine **17**(6), 573-581 (2006). doi:10.1007/s10856-006-8942-2
27. Xue, K., Teng, S.-H., Niu, N., Wang, P.: One-pot synthesis of novel tri-component composite microspheres of polyvinyl alcohol-silica-hydroxyapatite for biomedical applications. Materials Letters **257**, 126746 (2019). doi:https://doi.org/10.1016/j.matlet.2019.126746
28. Khurshid Z, Z.M., Qasim S, Shahab S, Naseem M, AbuReqaiba A.: Advances in Nanotechnology for Restorative Dentistry. Materials **8**(2), 717-731 (2015). doi:10.3390/ma8020717
29. Tian, T., Jiang, D., Zhang, J., Lin, Q.: Synthesis of Si-substituted hydroxyapatite by a wet mechanochemical method. Materials Science and Engineering: C **28**(1), 57-63 (2008).

doi:https://doi.org/10.1016/j.msec.2007.10.049

30. Yousefpour, M., Taherian, Z.: The effects of ageing time on the microstructure and properties of mesoporous silica-hydroxyapatite nanocomposite. Superlattices and Microstructures **54**, 78-86 (2013). doi:https://doi.org/10.1016/j.spmi.2012.11.002
31. Bogya, E.S., Károly, Z., Barabás, R.: Atmospheric plasma sprayed silica–hydroxyapatite coatings on magnesium alloy substrates. Ceramics International **41**(4), 6005-6012 (2015). doi:https://doi.org/10.1016/j.ceramint.2015.01.041
32. Wang, B., Zhang, J.-J., Pan, Z.-Y., Tao, X.-Q., Wang, H.-S.: A novel hydrogen peroxide sensor based on the direct electron transfer of horseradish peroxidase immobilized on silica–hydroxyapatite hybrid film. Biosensors and Bioelectronics **24**(5), 1141-1145 (2009). doi:https://doi.org/10.1016/j.bios.2008.06.053
33. Roh, J., Kim, J.-Y., Choi, Y.-M., Ha, S.-M., Kim, K.-N., Kim, K.-M.: Bone Regeneration Using a Mixture of Silicon-Substituted Coral HA and β-TCP in a Rat Calvarial Bone Defect Model. Materials (Basel) **9**(2), 97 (2016). doi:10.3390/ma9020097
34. Musi, S., Filipovi -Vincekovi, N., Sekovani, L.: Precipitation of amorphous SiO2 particles and their properties. Brazilian Journal of Chemical Engineering **28**, 89-94 (2011).
35. Pazarlioglu, S., Salman, S.: Effect of lanthanum oxide additive on the sinterability, physical/mechanical, and bioactivity properties of hydroxyapatite-alpha alumina composite. Journal of the Australian Ceramic Society **55**(4), 1195-1209 (2019). doi:10.1007/s41779-019-00336-4
36. Martínez, A., Izquierdo-Barba, I., Vallet-Regí, M.: Bioactivity of a CaO–SiO2 Binary Glasses System. Chemistry of Materials **12**(10), 3080-3088 (2000). doi:10.1021/cm001107o
37. Mote, V.D., Purushotham, Y., Dole, B.N.: Williamson-Hall analysis in estimation of lattice strain in nanometer-sized ZnO particles. Journal of Theoretical and Applied Physics **6**(1), 6 (2012). doi:10.1186/2251-7235-6-6
38. Schneider, J.-M., Bigerelle, M., Iost, A.: Statistical analysis of the Vickers hardness. Materials Science and Engineering: A **262**(1), 256-263 (1999). doi:https://doi.org/10.1016/S0921-5093(98)01000-4
39. Chicot, D., Mercier, D., Roudet, F., Silva, K., Staia, M.H., Lesage, J.: Comparison of instrumented Knoop and Vickers hardness measurements on various soft materials and hard ceramics. Journal of the European Ceramic Society **27**(4), 1905-1911 (2007). doi:https://doi.org/10.1016/j.jeurceramsoc.2006.06.011
40. Cahoon, J.R., Broughton, W.H., Kutzak, A.R.: The determination of yield strength from hardness measurements. Metallurgical Transactions **2**(7), 1979-1983 (1971). doi:10.1007/BF02913433
41. Mehdikhani, B., Borhani, G.H.: Densification and Mechanical Behavior of β-Tricalcium Phosphate Bioceramics. International Letters of Chemistry, Physics and Astronomy **36**, 37-49 (2014). doi:10.18052/www.scipress.com/ILCPA.36.37
42. Hung, I.M., Shih, W.-J., Hon, M.-H., Wang, M.-C.: The properties of sintered calcium phosphate with [Ca]/[P] = 1.50. International journal of molecular sciences **13**(10), 13569-13586 (2012). doi:10.3390/ijms131013569

43. Laasri, S., Taha, M., Hlil, E.K., Laghzizil, A., Hajjaji, A.: Manufacturing and mechanical properties of calcium phosphate biomaterials. Comptes Rendus Mécanique **340**(10), 715-720 (2012). doi:https://doi.org/10.1016/j.crme.2012.09.005
44. Singh, D., Salem, J., Halbig, M., Mathur, S.: Mechanical Properties and Performance of Engineering Ceramics and Composites VII. Wiley, (2012)
45. Furko, M., Bella, E.D., Fini, M., Balázsi, C.: Corrosion and biocompatibility examination of multi-element modified calcium phosphate bioceramic layers. Materials Science and Engineering: C **95**, 381-388 (2019). doi:https://doi.org/10.1016/j.msec.2018.01.010

Figures

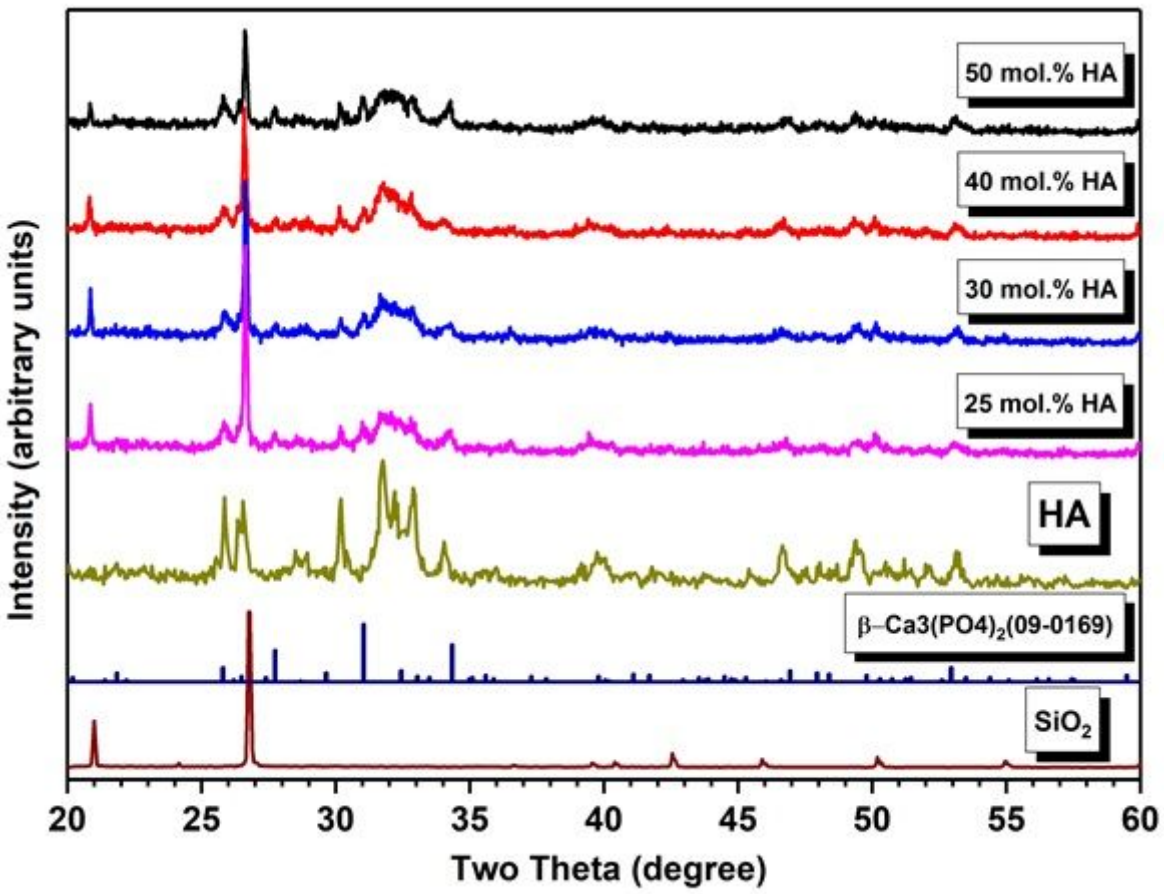

Figure 1

XRD patterns of silica with different HA content

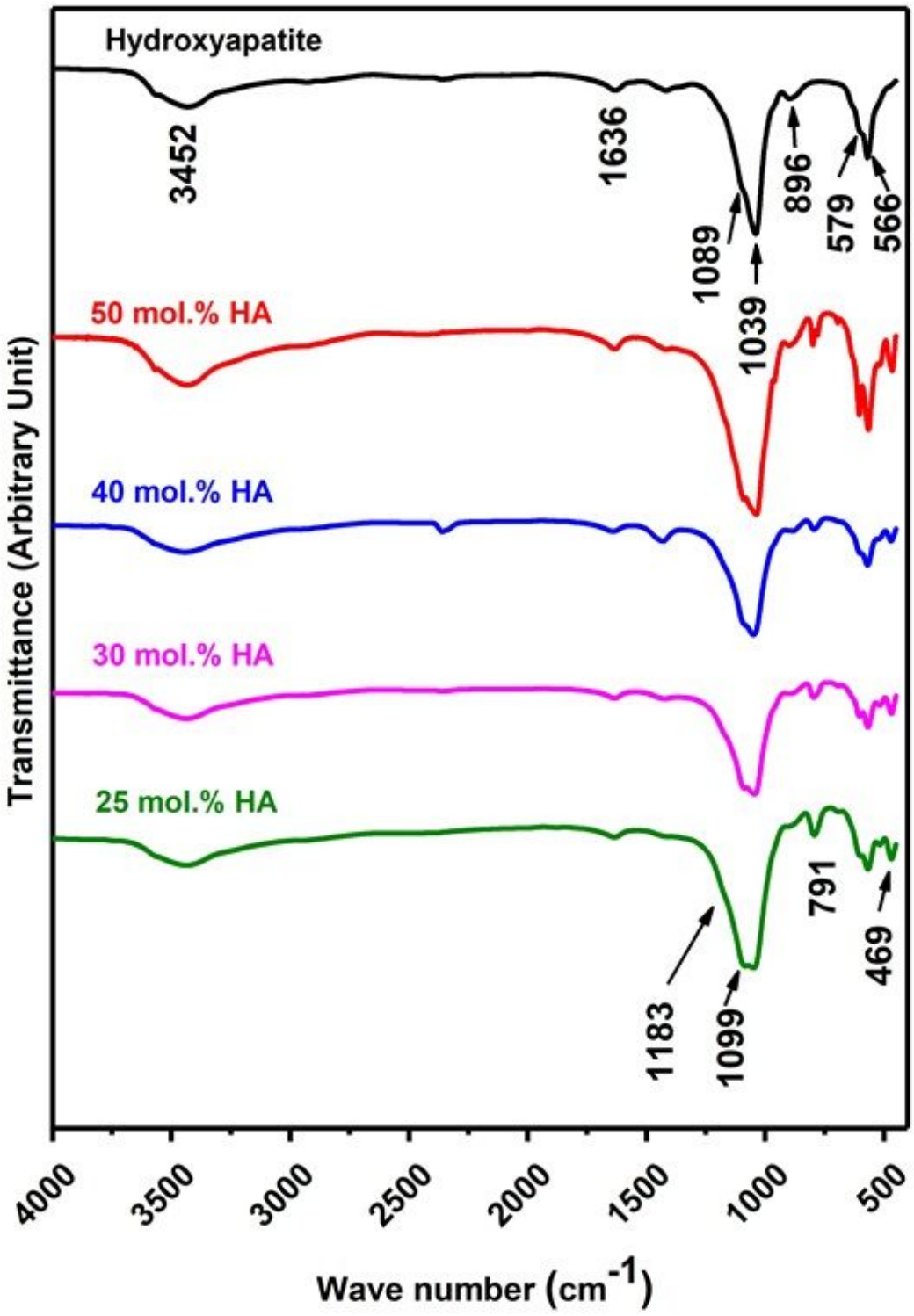

Figure 2

FT-IR spectrum of silica/HA after mechanical treatment.

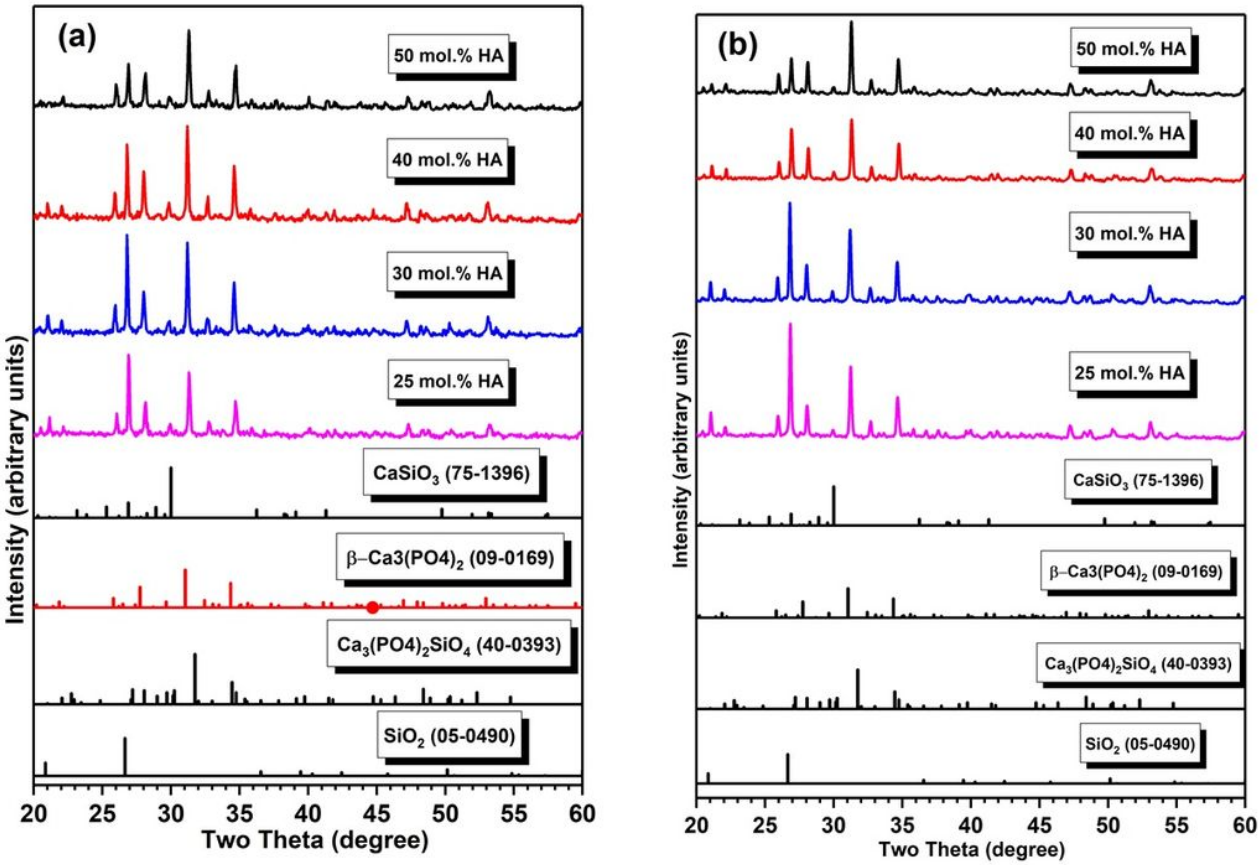

Figure 3

XRD patterns of heat-treated silica/HA at (a) 900oC and (b) 1200oC

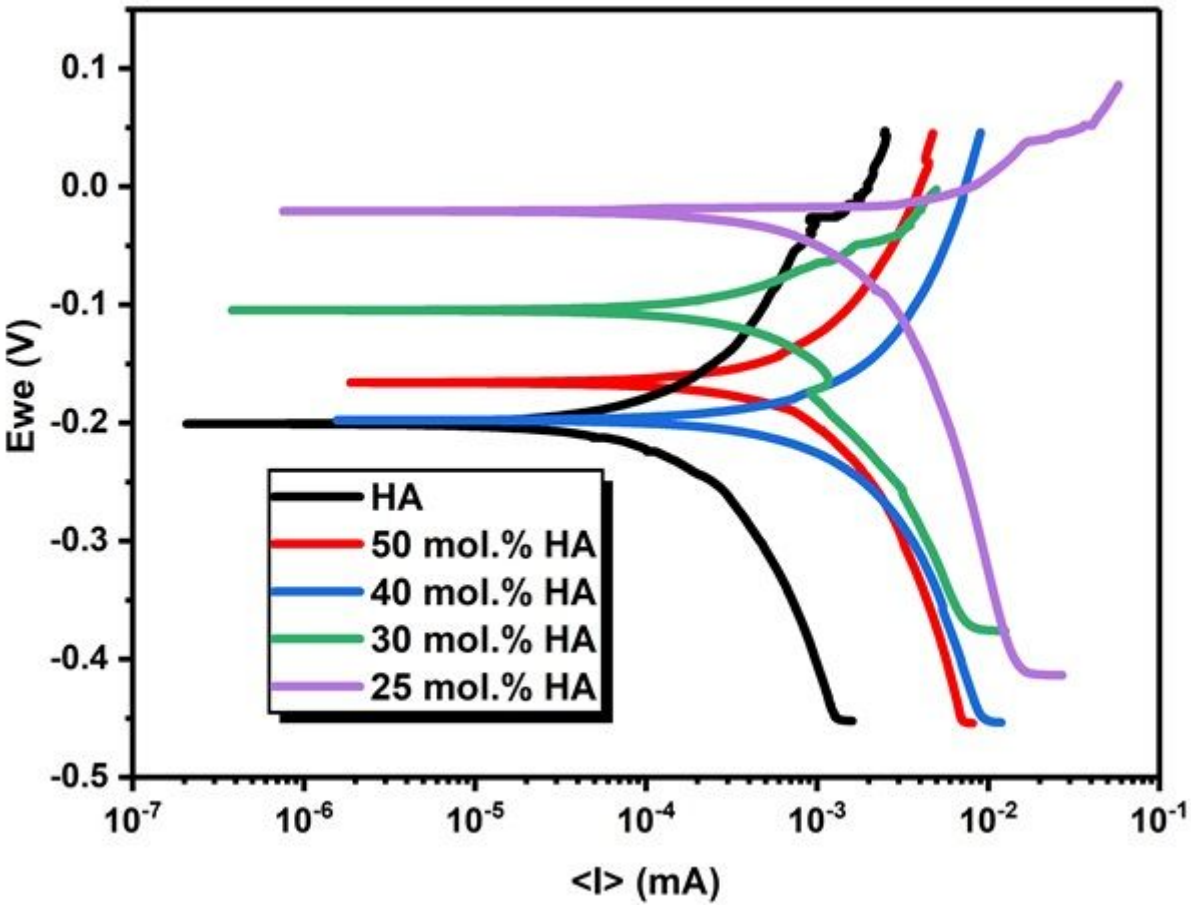

Figure 4

Polarization curves (Tafel diagram) of heat-treated HA and Silica/HA samples at 1200°C

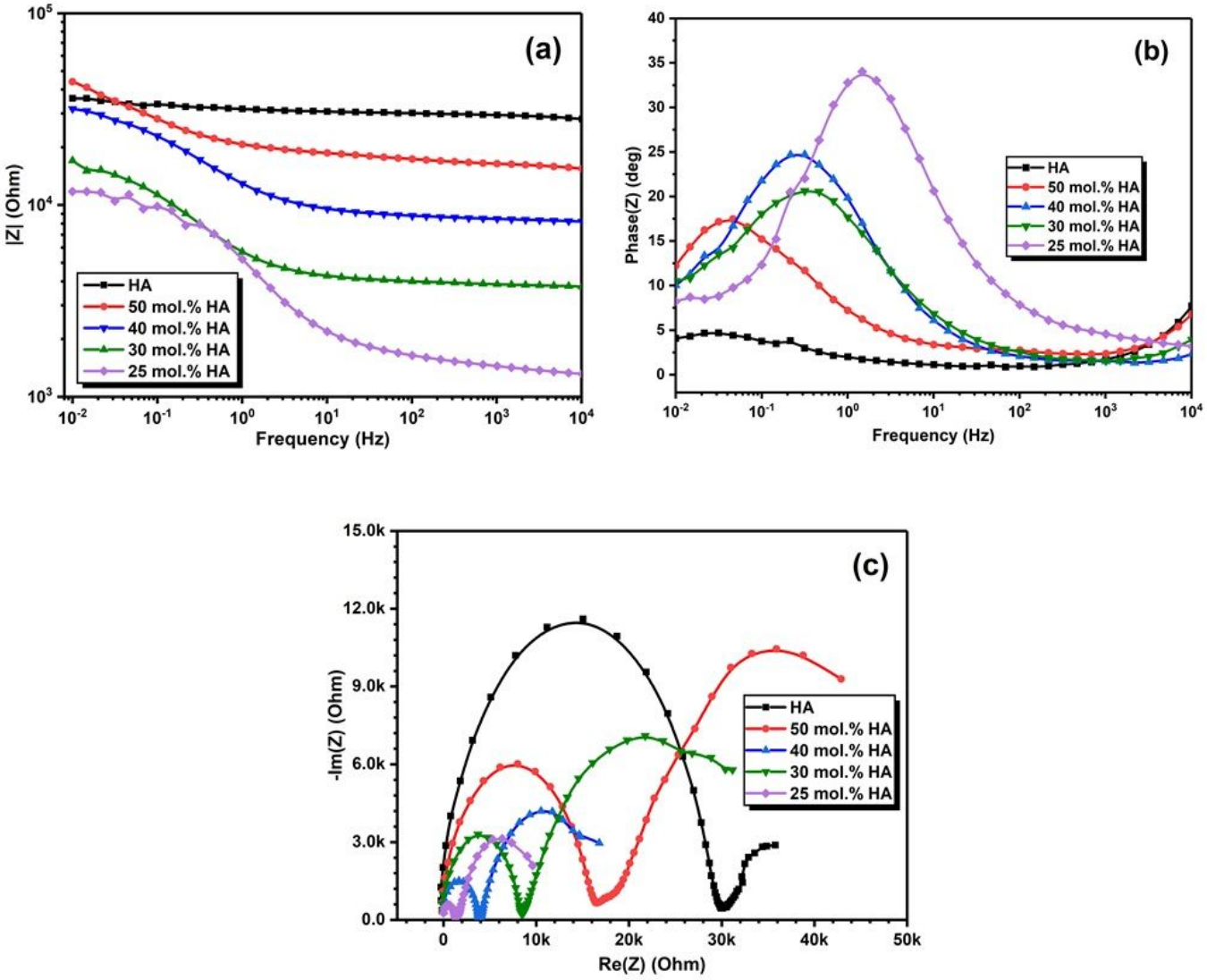

Figure 5

Complex impedance (Nyquist diagram) of heat-treated HA and Silica/HA samples at 1200°C